Bone 127 (2019) 244–249

Contents lists available at ScienceDirect

Bone

journal homepage: www.elsevier.com/locate/bone

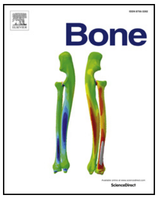

Rapid Communication

Extracellular matrix composition during bone regeneration in the human dental alveolar socket

Furqan A. Shah[a,*,1], Shariel Sayardoust[a,b,1], Peter Thomsen[a], Anders Palmquist[a]

[a] *Department of Biomaterials, Sahlgrenska Academy, University of Gothenburg, Gothenburg, Sweden*
[b] *Department of Periodontology, Institute for Postgraduate Dental Education, Jönköping, Sweden*

ARTICLE INFO

Keywords:
Bone
Dental alveolar socket
Extracellular matrix
Bone regeneration
Raman spectroscopy
Osteocyte

ABSTRACT

Within the dental alveolar socket, the sequence of events following tooth extraction involves deposition of a provisional connective tissue matrix that is later replaced by woven bone and eventually by lamellar bone. Bone regeneration within the dental alveolar socket is unique since the space occupied by the root(s) of a tooth does not originally contain any bone. However, extracellular matrix composition of the healing alveolar socket has not previously been investigated. Here, alveolar bone biopsies representing early (7–46 months, < *4y*) and late (48–60 months; *4–5y*) healing periods were investigated using Raman spectroscopy, X-ray micro-computed tomography and backscattered electron scanning electron microscopy. Partially or completely edentulous individuals and those with a smoking habit were *not* excluded. Between < *4y* and *4–5y*, mineral crystallinity and bone mineral density increase, phenylalanine, proline/hydroxyproline, and bone surface-to-volume ratio decrease, while the carbonate-to-phosphate ratio, the mineral-to-matrix ratio, and the collagen crosslink ratio remain relatively unchanged. Observed exclusively at *4–5y*, hypermineralised osteocyte lacunae contain spherical and rhomboidal mineral nodules. Spearman correlation analysis reveals several significant, high ($\rho = 0.7$–0.9; $p \leq 0.01$) and moderate ($\rho = 0.5$–0.7; $p \leq 0.01$) correlations. Mineral crystallinity and proline/hydroxyproline, the carbonate-to-phosphate ratio and phenylalanine, mineral crystallinity and bone surface-to-volume ratio, the carbonate-to-phosphate ratio and bone surface-to-volume ratio, proline/hydroxyproline and bone mineral density, and bone mineral density and bone surface-to-volume ratio are negatively correlated. Mineral crystallinity and bone mineral density, and proline/hydroxyproline and bone surface-to-volume ratio are positively correlated. Although bone regeneration in the dental alveolar socket follows typical bone healing patterns, the compositional and microstructural patterns reveal mature bone at < *4y* with indications of better mechanical competence at *4–5y*.

1. Introduction

Bone regeneration within the dental alveolar socket is a unique event since the space previously occupied by the root(s) of a tooth does not characteristically contain any bone. Sharpey's fibres of the periodontal ligament are embedded into the *alveolar bone proper*, which closely surrounds the roots in the form of a thin collar but is gradually resorbed after tooth extraction [1]. Following tooth extraction, bone regeneration within the alveolar socket is reminiscent of fracture healing, beginning with the deposition of a provisional connective tissue matrix that is later replaced by woven bone and eventually by lamellar bone [2]. Replacement of lost or missing teeth is often undertaken using osseointegrated implants, which restore not only facial aesthetics but also dental function. Prior to implant placement, various arbitrary recommendations for the duration of post-extraction healing are followed in order to ensure primary stability and to achieve osseointegration. An implant is inserted when radiographic bone density in the alveolar socket is deemed to be *satisfactory*. Nevertheless, the alveolar ridge suffers reduction in both vertical and horizontal dimensions, which is challenging to prevent even with immediate implant placement in fresh extraction sockets [3].

As a hierarchical material [4], the physical properties of bone are governed by the combination of material composition and the unique multiscale architecture [5]. Comprehensive understanding of healing kinetics and factors that influence bone quality is, therefore, critical for accurate clinical decision making, particularly since the time needed for complete healing varies considerably between individuals [1,6,7]. Histologically, the alveolar process is comprised of lamellar bone,

---

[*] Corresponding author.
E-mail address: furqan.ali.shah@biomaterials.gu.se (F.A. Shah).
[1] These authors contributed equally to this work.

https://doi.org/10.1016/j.bone.2019.06.003
Received 1 April 2019; Received in revised form 3 June 2019; Accepted 6 June 2019

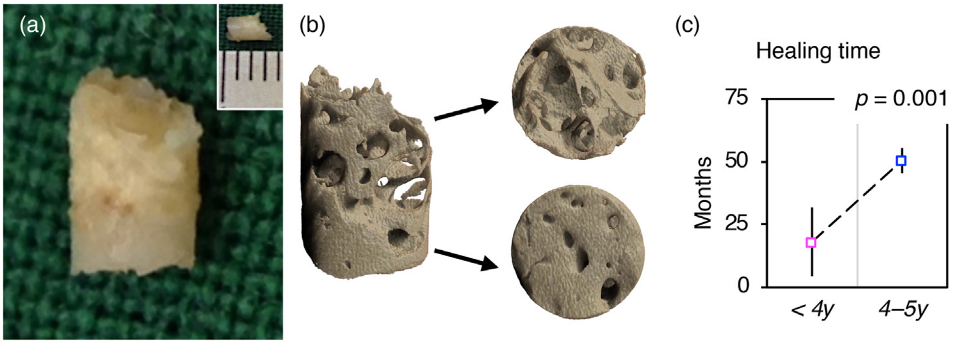

Fig. 1. Alveolar bone biopsies. (a) Photograph of an alveolar bone biopsy. (b) X-ray micro-computed tomography reconstruction of the same sample. (c) Healing time.

woven bone, osteoid, bone marrow, and fibrous tissue in varying proportions [8]. However, little is known about the molecular level composition of the extracellular matrix during alveolar socket healing. To this end, we report the (*i*) extracellular matrix composition and (*ii*) bone microstructure, using Raman spectroscopy, X-ray micro-computed tomography, and backscattered electron scanning electron microscopy, including parameters that represent the degree of tissue organisation, maturity/age, mechanical competence, and available surface for bone remodelling.

2. Materials and methods

Alveolar bone biopsies were collected from 30 systemically healthy individuals (Table S1), between 7 and 60 months after tooth extraction due to dental caries, cracked teeth, endodontic problems, and periodontitis. These biopsies were categorised as early (< *4y*; 18 ± 14 months; $n = 11$) and late (*4–5y*; 51 ± 5 months; $n = 19$) healing (Fig. 1). The study protocol was approved by the Institutional Review Board at the University of Linköping (Dnr 2016/319–31). Informed consent was obtained from all participants. The study was conducted in accordance with the guidelines of Good Clinical Practice for Trials on Medicinal Products in the European Community, the International Conference on Harmonisation (ICH) guideline for Good Clinical Practice, the Declaration of Helsinki, and the CONSORT guidelines for clinical studies.

The study subjects were selected from patients, male and female, aged between 35 and 72 years, referred to the Department of Periodontology, Institute for Postgraduate Dental Education, Jönköping, Sweden, between January 2016 and January 2017 for dental implant placement at least six months after tooth extraction. Additional inclusion criteria were: (*i*) adequate volume of alveolar bone for implant placement, according to the Lekholm and Zarb classification [9], and (*ii*) absence of risk factors that may affect levels of bone-related gene expression, including osteoporosis, chronic use of anti-inflammatory agents, use of bisphosphonates, or severe metabolic diseases such as diabetes mellitus. Partially or completely edentulous individuals, and those with a smoking habit were *not* excluded. Cylindrical, 2 × 3 mm, alveolar bone biopsies were obtained under local anaesthesia from premolar regions using a trephine drill and were immediately immersed in 10% neutral buffered formalin, followed by dehydration in a graded ethanol series (50–100%) and resin embedding (LR White, London Resin Co. Ltd., UK).

2.1. Bone microstructure

Using X-ray micro-computed tomography (micro-CT), bone mineral density (BMD) and bone surface-to-volume ratio (BS/BV) were evaluated. All samples were scanned over a 180° rotation at a step size of 0.5° with an average of four frames and an image pixel size of 7.92 μm in a Skyscan 1172 (Bruker micro-CT, Kontich, Belgium) operating at 49 kV energy with an Al filter (0.5 mm). BMD calibration phantoms (0.25 g/cm^3 and 0.75 g/cm^3 stoichiometric hydroxyapatite in epoxy resin, 2 mm diameter) were also scanned using the same settings. Reconstruction, analysis, and visualisation were performed using associated Skyscan software (NRecon, Image viewer, CTVox, CTAn).

Resin embedded blocks were wet polished using 400–4000 grit SiC paper for backscattered electron scanning electron microscopy (BSE-SEM) in a Quanta 200 environmental SEM operated at 20 kV accelerating voltage, 1 Torr water vapour pressure, and 10 mm working distance.

2.2. Extracellular matrix composition

Raman spectroscopy was performed using a confocal Raman microscope (WITec alpha300 R, Ulm, Germany), equipped with a 532 nm laser. The composition of the extracellular matrix was analysed at 20 × 20 μm regions of interest. Between 8 and 10 locations were analysed on each sample. On the surface of polished resin embedded blocks, the laser was focused down on to the sample using a ×100 objective having a numerical aperture of 0.9. Spectra were collected in the 300–1800 cm^{-1} spectral range behind a 600 mm^{-1} grating, at a spectral resolution of ~6 cm^{-1}, an integration time of 3 s per pixel, and an isotropic pixel size of 5 μm. Background fluorescence subtraction was performed in WITEC Control FIVE software. Curve fitting and quantification of integral areas was done using MagicPlot (www.magicplot.com). The integral areas were: ν_1 PO_4^{3-} (960 ± 15 cm^{-1}), ν_2 PO_4^{3-} (437 ± 25 cm^{-1}), ν_1 CO_3^{2-} (1072 ± 15 cm^{-1}), Amide III (1259 ± 40 cm^{-1}), Amide I (1660 ± 40 cm^{-1}), and Pro + Hyp (850 ± 30 cm^{-1}). The Raman metrics investigated included mineral crystallinity, taken as the reciprocal of the full-width at half-maximum (1/FWHM) of the ν_1 PO_4^{3-} peak, the carbonate-to-phosphate ratio (ν_1 CO_3^{2-}/ν_2 PO_4^{3-}), the mineral-to-matrix ratio (ν_2 PO_4^{3-}/Amide III), and the collagen crosslink ratio (CXLR), taken as the percentage area of the Amide I sub-component at ~1662 cm^{-1} [10]. To identify sub-component peaks in the Amide I region, second derivative spectra were calculated, followed by deconvolution of the 1540–1740 cm^{-1} envelope by fitting Gaussian curves centred at ~1555 cm^{-1}, ~1572 cm^{-1}, ~1589 cm^{-1}, ~1604 cm^{-1}, ~1616 cm^{-1}, ~1621 cm^{-1}, ~1638 cm^{-1}, ~1662 cm^{-1}, ~1669 cm^{-1}, ~1691 cm^{-1}, ~1708 cm^{-1}, ~1720 cm^{-1}, and ~1736 cm^{-1}. The amount of amino acid phenylalanine relative to the main phosphate peak at 959 cm^{-1} (Phe/ν_1 PO_4^{3-}) and the amount of amino acids proline/hydroxyproline (Pro + Hyp) were also investigated.

2.3. Statistical analysis

The Kruskall–Wallis test was used for all statistical analyses between < *4y* and *4–5y* groups; p values < 0.05 were considered statistically significant. Mean values ± standard deviations are shown. Spearman correlation analysis was performed (data pooled for < *4y*

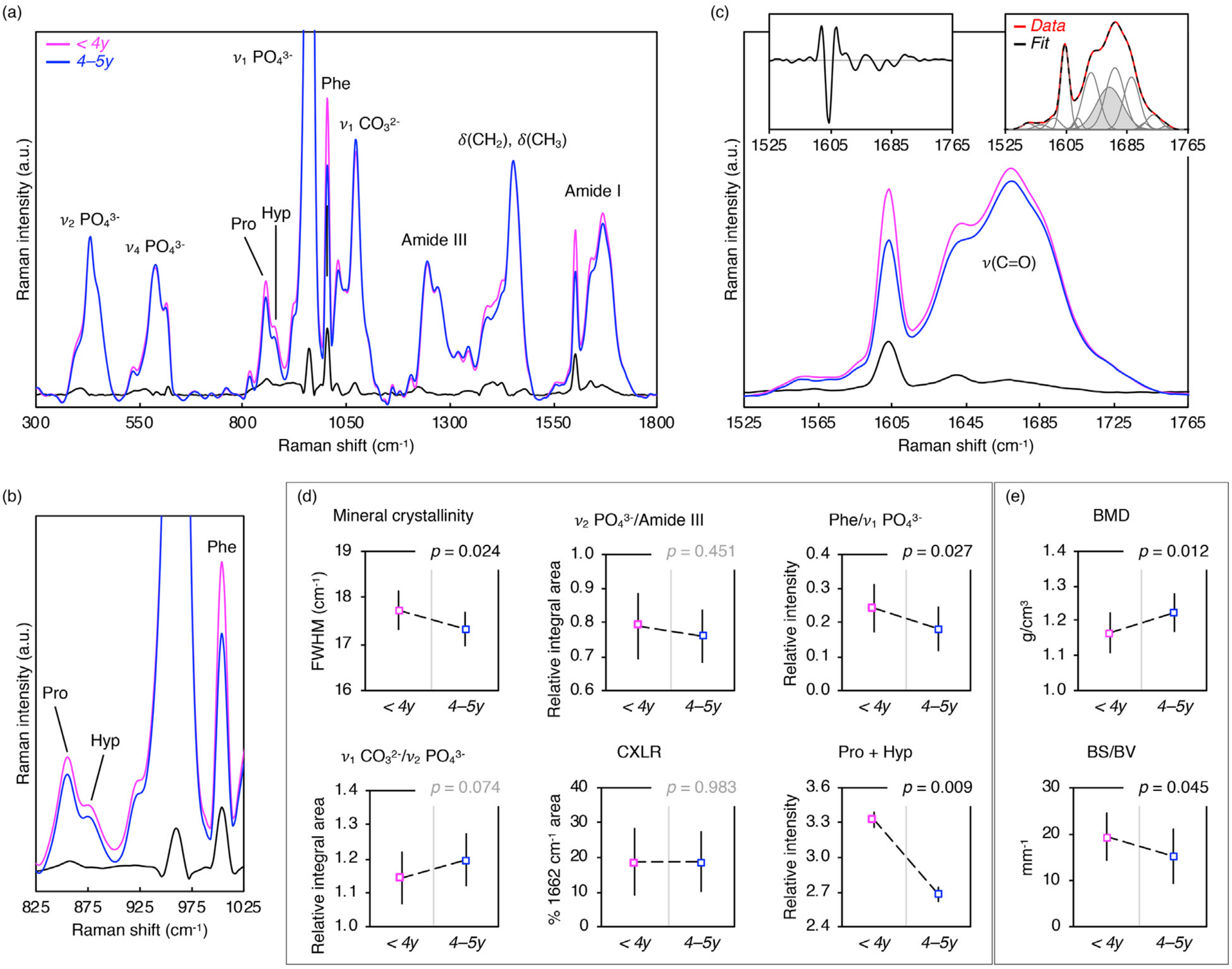

Fig. 2. (a) Average Raman spectra of < *4y* (*n* = 11) and *4–5y* (*n* = 19) groups and the absolute difference Raman spectrum (black line). Spectra are normalised to the intensity of the 1453 cm^{-1} peak. (b) Detail of the 825–1025 cm^{-1} spectral region showing the Pro + Hyp and Phe bands and the absolute difference Raman spectrum (black line). (c) Detail of the 1525–1765 cm^{-1} spectral region showing the Amide I band and the absolute difference Raman spectrum (black line). Insets: Second derivative spectrum (left) for identification of sub-component peaks in the Amide I region and sub-component deconvolution of the 1540–1740 cm^{-1} envelope by Gaussian curve fitting (right). The percentage area of the Amide I sub-component at ~1662 cm^{-1} represents the collagen crosslink ratio. (d) Raman metrics for extracellular matrix composition. (e) Microstructural parameters.

and *4–5y*) between healing time, FWHM ν_1 PO_4^{3-}, ν_1 CO_3^{2-}/ν_2 PO_4^{3-}, ν_2 PO_4^{3-}/Amide III, CXLR, Phe, Pro + Hyp, BMD, and BS/BV. Based on the value of the Spearman's rank correlation coefficient, ρ, the strength of the correlation is interpreted as: little if any correlation (0.0–0.3), low (0.3–0.5), moderate (0.5–0.7), high (0.7–0.9), and very high (0.9–1.0) [11]; *p* values < 0.01 were considered statistically significant. The correlation coefficient, ρ, and the statistical significance level, *p*, are provided.

3. Results

3.1. Mineral crystallinity and bone mineral density increase with healing time

The Raman spectral features at both < *4y* and *4–5y* healing were consistent with those of mineralised bone (Fig. 2). At *4–5y,* the mineral crystallinity (1/FWHM ν_1 PO_4^{3-}) was significantly higher ($p = 0.024$) than at < *4y*. In contrast, Phe ($p = 0.027$) and Pro + Hyp ($p = 0.009$) decreased between < *4y* and *4–5y* healing. The carbonate-to-phosphate ratio (ν_1 CO_3^{2-}/ν_2 PO_4^{3-}), the mineral-to-matrix ratio (ν_2 PO_4^{3-}/Amide III), and the collagen crosslink ratio (CXLR) did not change significantly beyond < *4y* healing. In addition to extracellular matrix composition, the bone mineral density (BMD) increased ($p = 0.012$) while the bone surface-to-volume ratio (BS/BV) decreased ($p = 0.045$) between < *4y* and *4–5y* healing.

3.2. Hypermineralised osteocyte lacunae at late healing

Almost exclusively at *4–5y* healing, BSE-SEM revealed that a small proportion of osteocyte lacunae were hypermineralised and contained equiaxed mineral nodules that were mainly spherical, including a few with a fuzzy exterior (Fig. 3). Rhomboidal, distinctly facetted, nodules were also noted. Frequently, a hypermineralised ring enclosed the lacuna.

3.3. Correlation analysis

Spearman correlation analysis revealed several significant correlations (Table 1). High correlations were found between FWHM ν_1 PO_4^{3-} and Pro + Hyp ($\rho = 0.851$, $p = 0.001$) and ν_1 CO_3^{2-}/ν_2 PO_4^{3-} and Phe ($\rho = -0.790$, $p = 0.001$). Moderate correlations were found between BMD and BS/BV ($\rho = -0.649$, $p = 0.001$), FWHM ν_1 PO_4^{3-} and BMD ($\rho = -0.699$, $p = 0.001$), FWHM ν_1 PO_4^{3-} and BS/BV ($\rho = 0.655$, $p = 0.001$), ν_1 CO_3^{2-}/ν_2 PO_4^{3-} and BS/BV ($\rho = -0.527$, $p = 0.003$), Pro + Hyp and BMD ($\rho = -0.574$, $p = 0.001$), and Pro + Hyp and BS/BV ($\rho = 0.546$, $p = 0.002$).

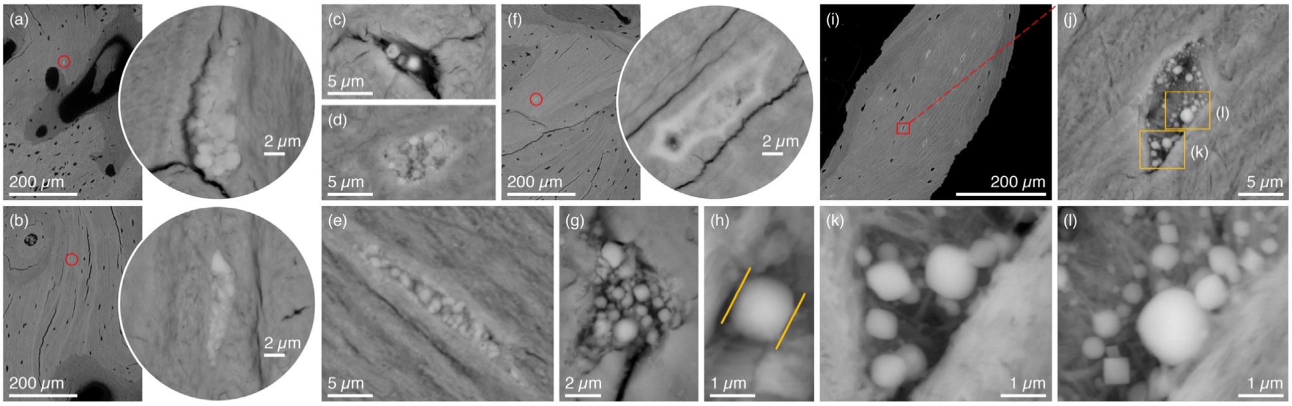

Fig. 3. Hypermineralised osteocyte lacunae (*4–5y*). (a) 48 months. Spherical mineral nodules. Boundaries of individual mineral nodules are visible. (b) 60 months. Mineral nodules are partially coalesced and there is a minor contrast difference between the mineralised lacuna and the surrounding tissue. (c) Spherical nodules with a fuzzy exterior. (d) Some nodules exhibit a distinct core–shell structure. (e) A hypermineralised ring surrounds the lacuna. (f) Hypermineralisation extends into the canalicular space. (g) Rhomboidal mineral nodules. (h) A solitary rhomboidal nodule. (i) A trabecula containing many hypermineralised lacunae. (j–l) A selected hypermineralised lacuna having both spherical nodules and distinctively facetted rhomboidal nodules.

4. Discussion

Constituents of the extracellular matrix contribute greatly to the strength and mechanical competence of bone [12]. Following tooth extraction, alveolar socket healing involves a sequence of events similar to fracture healing [2]. In agreement with these histological observations, the mineral crystallinity (1/FWHM ν_1 PO_4^{3-}), which represents several factors, e.g., crystallite size and atomic scale disorder, was found to increase with healing time. With increasing tissue age, the width of the ν_1 PO_4^{3-} peak decreases [13], while the ν_1 CO_3^{2-} band intensity increases relative to the ν_1 PO_4^{3-} peak [14]. For synthetic apatites, greater CO_3^{2-} substitution typically results in ν_1 PO_4^{3-} peak broadening [15]. However, this trend is not always observed in bone. One explanation is that the precision with which mineral crystallinity can be measured is poor, because the range of bandwidths observed for a given tissue type is small (~1–3 cm^{-1}) [16]. Moreover, since collagen acts as a structural template that controls nucleation, growth, and orientation of bone apatite [17], continued crystal growth along the *c*-axis compensates for the effect of CO_3^{2-} substitution [18].

Simultaneously, Phe and Pro + Hyp decreased between < *4y* and *4–5y*, indicating that minor changes in the organic phase may occur independently of the mineral phase. Furthermore, absence of a corresponding change in the ν_2 PO_4^{3-}/Amide III ratio implies a steady-state of bone remodelling. The Phe peak, at 1004 cm^{-1}, has been used as a measure of organic constituents of the extracellular matrix [19]. Based on our previous work, Phe levels tend to decrease with increasing tissue age [20] and have been recorded at around 9–12% with respect to the intensity of the phosphate peak at 960 cm^{-1} in alveolar bone [21,22]. Phe levels here are markedly higher, ~24 ± 7.1% at < *4y* and ~18 ± 6.6% at *4–5y*, which indicates the presence of woven bone remnants.

The volume fractions of individual constituents of composite materials, i.e., carbonated apatite and type-I collagen in bone, directly influence the physical properties. Using the *rule of mixtures* equation, it is possible to predict the Young's modulus of the extracellular matrix assuming weighted contributions from the constituent phases. The mineral fraction values, as estimated from the mineral-to-matrix ratios, are ~0.440 ± 0.03 at < *4y* and ~0.431 ± 0.03 at *4–5y*. Atomistic simulations suggest that at a mineral density of ~30%, a mineralised collagen fibril reaches maximum elastic modulus [23]. With the mineral fractions at < *4y* and *4–5y* being similar, amongst other compositional parameters including collagen crosslink ratios and carbonate-to-phosphate ratios that were also comparable, it is reasonable to assume that the extracellular matrix exhibits high mechanical

Table 1
Spearman correlation analysis between healing time, microstructural parameters, and compositional parameters.

	FWHM *ν_1 PO_4^{3-}*	*ν_1 CO_3^{2-}/* *ν_2 PO_4^{3-}*	*ν_2 PO_4^{3-}/* *Amide III*	*CXLR*	*Phe/* *ν_1 PO_4^{3-}*	*Pro + Hyp*	*BMD*	*BS/BV*	
Healing time	−0.33	0.409*	−0.07	0.080	−0.373*	−0.463**	0.374*	−0.272	ρ
	0.075	0.025	0.714	0.673	0.043	0.01	0.041	0.146	*p*
FWHM		−0.371*	−0.13	0.209	0.332	0.851**	−0.699**	0.655**	ρ
ν_1 PO_4^{3-}		0.043	0.495	0.267	0.073	0.000	0.000	0.000	*p*
ν_1 CO_3^{2-}/			−0.317	0.308	−0.790**	−0.483**	0.258	−0.527**	ρ
ν_2 PO_4^{3-}			0.088	0.098	0.000	0.007	0.168	0.003	*p*
ν_2 PO_4^{3-}/				−0.349	0.437*	−0.309	0.241	0.004	ρ
Amide III				0.058	0.016	0.096	0.199	0.982	*p*
CXLR					−0.339	0.125	−0.386*	0.065	ρ
					0.067	0.510	0.035	0.732	*p*
Phe/						0.440*	−0.214	0.464**	ρ
ν_1 PO_4^{3-}						0.015	0.257	0.01	*p*
Pro + Hyp							−0.574**	0.546**	ρ
							0.001	0.002	*p*
BMD								−0.649**	ρ
								0.000	*p*

ρ = Spearman's rank correlation coefficient.
** Significant at the *p* = 0.01 level.
* Significant at the *p* = 0.05 level.

competence at ~18 months healing, which improves only slightly by ~51 months if the increase in mineral crystallinity is also considered.

The strength of bone is governed not only by the mineral content, but is also influenced by the degree of mineral crystallinity [16,24]. Increase in mineral crystallinity with simultaneous BMD increase and BS/BV decrease may be explained as a thermodynamically driven surface dissolution and recrystallisation of the existing mineral while new mineral is being added. Therefore, an increase in mineral crystallinity, attributed to continued crystal growth and progressively greater apatite occupancy of inter- and intrafibrillar spaces, will directly contribute to an increase in the BMD. Owing to broken bonds and charge imbalance, single-crystals exhibit a strained surface zone and distorted underlying atomic geometry. This deformed surface zone, in nano-sized crystals, comprises a large proportion of the crystallite volume [25]. Crystal growth, therefore, leads to reduction in the surface-to-volume ratio, which is detectable as a sharpening of the ν_1 $PO_4{}^{3-}$ peak. Together with the increase in BMD, the observed decrease in BS/BV may be attributed to progressive reduction in micrometre-scale porosities (e.g., osteocyte lacunae and blood vessels). BS/BV has been shown to correlate negatively with fracture toughness (K_c) [26]. A negative correlation between ν_1 $CO_3{}^{2-}$/ν_2 $PO_4{}^{3-}$ and BS/BV, therefore, suggests that carbonate ion incorporation may be associated with increased resistance to crack propagation. In biological apatites, $CO_3{}^{2-}$ substitution for $PO_4{}^{3-}$ affects various physical properties including crystallite size, solubility, and thermal stability [27], effectively limiting mineral crystallinity to less than that observed for carbonate-free apatites.

The secondary structure of collagen, such as the characteristic triple helix (or 3_{10}-helix) [28], can be interpreted from the Amide I band [29,30]. The arrangement of collagen molecules within a fibril is governed by intermolecular crosslinking [10]. Collagen crosslinking and the resultant molecular structure impart tensile strength and viscoelastic behaviour to the fibrillar collagen matrix in mineralised tissues [31,32]. Even when limited to microanatomical locations, alterations in collagen crosslinking can affect the mechanical competence on the whole bone level, independent of changes in the mineral phase [33]. The collagen crosslink ratio, considered here as the % area of the $1662\,cm^{-1}$ sub-component, represents pyridinoline (or hydroxylysylpyridinoline) crosslinks in collagen [10]. Here, collagen crosslinking was not observed to change significantly between < *4y* and *4–5y*.

Hypermineralised osteocyte lacunae, which were never observed at < *4y* healing, provide additional evidence for a temporal change in the mechanical properties at the tissue level. It has been shown that hardness and reduced elastic modulus of such mineral nodules can be ~120% and ~50%, respectively, greater than the mineralised extracellular matrix, while the different morphologies represent different calcium phosphate phases [22]. Originally referred to as '*micropetrosis*' [34], hypermineralised osteocyte lacunae contain apoptotic debris [35,36], and are a hallmark feature of the ageing skeleton [37]. When present in large numbers, such localised regions of hypermineralisation may contribute directly to increased fragility and embrittlement of bone [38], and speculatively through a decreased capacity to sense loading, detect microdamage, and orchestrate bone remodelling [39]. Furthermore, the presence of hypermineralised osteocyte lacunae may be linked to increased osteocyte apoptosis as a consequence of low mechanical stimuli, particularly in the case of unloaded alveolar bone.

A potential limitation of this work is chemical fixation using formalin, which is considered sub-optimal for spectroscopic analysis of bone. Various compositional parameters may be affected compared to other fixation methods (e.g., 70–100% ethanol, glycerol etc.) and unprocessed and/or cryo-sectioned tissues [40]. The inclusion of smokers may also be considered a limitation. Histologically, the proportions of lamellar bone, woven bone, osteoid, bone marrow, and fibrous tissue in alveolar bone do not differ significantly between individuals with and without a smoking habit [8], but it is currently not known if smoking alters extracellular matrix composition or delays the healing process.

5. Conclusions

Bone regeneration in the dental alveolar socket follows typical bone healing patterns. Although the extracellular matrix may be considered compositionally and microstructurally mature at < *4y* healing, increases in mineral crystallinity and BMD, and decreases in Phe, Pro + Hyp, and BS/BV are detected as late as *4–5y* healing. Hypermineralised osteocyte lacunae are observed exclusively at *4–5y* healing, and contain predominantly spherical but also rhomboidal mineral nodules, occasionally.

Supplementary data to this article can be found online at https://doi.org/10.1016/j.bone.2019.06.003.

Acknowledgements

The authors wish to thank Lena Emanuelsson and Märta-Sofie Geijer for technical assistance. Financial support is acknowledged from the Swedish Research Council (2018-02891), Svenska Sällskapet för Medicinsk Forskning (SSMF) postdoctoral scholarship, the Swedish state under the agreement between the Swedish government and the county councils, the ALF agreement (ALFGBG-725641), the Adlerbertska Foundation, the IngaBritt and Arne Lundberg Foundation, the Wilhelm and Martina Lundgren Foundation, Stiftelsen Konrad och Helfrid Johanssons fond, the Dr. Felix Neubergh Foundation, Promobilia, the Hjalmar Svensson Foundation, Futurum – Academy for Health and Care, Jönköping County Council, Jönköping, the Osteology Foundation (YRG 17-047), and the Materials Science Area of Advance at Chalmers and the Department of Biomaterials, University of Gothenburg within the Strategic Research Area initiative launched by the Swedish Government.

References

[1] M.G. Araújo, C.O. Silva, M. Misawa, F. Sukekava, Alveolar socket healing: what can we learn? Periodontol 2000 (68) (2015) 122–134.
[2] G. Cardaropoli, M. Araújo, J. Lindhe, Dynamics of bone tissue formation in tooth extraction sites. An experimental study in dogs, J. Clin. Periodontol. 30 (2003) 809–818.
[3] M.G. Araújo, J.L. Wennström, J. Lindhe, Modeling of the buccal and lingual bone walls of fresh extraction sites following implant installation, Clin. Oral Implants Res. 17 (2006) 606–614.
[4] P. Fratzl, R. Weinkamer, Nature's hierarchical materials, Prog. Mater. Sci. 52 (2007) 1263–1334.
[5] E. Seeman, P.D. Delmas, Bone quality—the material and structural basis of bone strength and fragility, N. Engl. J. Med. 354 (2006) 2250–2261.
[6] L. Trombelli, R. Farina, A. Marzola, L. Bozzi, B. Liljenberg, J. Lindhe, Modeling and remodeling of human extraction sockets, J. Clin. Periodontol. 35 (2008) 630–639.
[7] K. Bertl, E.B. Kukla, R. Albugami, F. Beck, A. Gahleitner, A. Stavropoulos, Timeframe of socket cortication after tooth extraction: a retrospective radiographic study, Clin. Oral Implants Res. 29 (2018) 130–138.
[8] J. Lindhe, D. Cecchinato, E.A. Bressan, M. Toia, M.G. Araújo, B. Liljenberg, The alveolar process of the edentulous maxilla in periodontitis and non-periodontitis subjects, Clin. Oral Implants Res. 23 (2012) 5–11.
[9] U. Lekholm, G.A. Zarb, Patient selection and preparation, in: P.I. Brånemark, G.A. Zarb, A. T (Eds.), Tissue Integrated Prostheses: Osseointegration in Clinical Dentistry. Chicago, Ill, USA: Quintessence, 1985, pp. 199–209.
[10] S. Gamsjaeger, S.P. Robins, D.N. Tatakis, K. Klaushofer, E.P. Paschalis, Identification of pyridinoline trivalent collagen cross-links by Raman microspectroscopy, Calcif. Tissue Int. 100 (2017) 565–574.
[11] D.E. Hinkle, W. Wiersma, S.G. Jurs, Applied Statistics for the Behavioral Sciences, 5th ed., Boston, MA, Houghton Mifflin, 2003.
[12] Y. Bala, E. Seeman, Bone's material constituents and their contribution to bone strength in health, disease, and treatment, Calcif. Tissue Int. 97 (2015) 308–326.
[13] J.J. Freeman, B. Wopenka, M.J. Silva, J.D. Pasteris, Raman spectroscopic detection of changes in bioapatite in mouse femora as a function of age and in vitro fluoride treatment, Calcif. Tissue Int. 68 (2001) 156–162.
[14] O. Akkus, F. Adar, M.B. Schaffler, Age-related changes in physicochemical properties of mineral crystals are related to impaired mechanical function of cortical bone, Bone 34 (2004) 443–453.
[15] J.-D.P. McElderry, P. Zhu, K.H. Mroue, J. Xu, B. Pavan, M. Fang, G. Zhao, E. McNerny, D.H. Kohn, R.T. Franceschi, M.M.B. Holl, M.M.J. Tecklenburg, A. Ramamoorthy, M.D. Morris, Crystallinity and compositional changes in carbonated apatites: evidence from 31P solid-state NMR, Raman, and AFM analysis, J. Solid State Chem. 206 (2013) 192–198.
[16] M.D. Morris, G.S. Mandair, Raman assessment of bone quality, Clin. Orthop. Relat.

Res. 469 (2011) 2160–2169.
[17] Y. Wang, T. Azais, M. Robin, A. Vallee, C. Catania, P. Legriel, G. Pehau-Arnaudet, F. Babonneau, M.M. Giraud-Guille, N. Nassif, The predominant role of collagen in the nucleation, growth, structure and orientation of bone apatite, Nat. Mater. 11 (2012) 724–733.
[18] J.S. Yerramshetty, C. Lind, O. Akkus, The compositional and physicochemical homogeneity of male femoral cortex increases after the sixth decade, Bone 39 (2006) 1236–1243.
[19] J.D. McElderry, G. Zhao, A. Khmaladze, C.G. Wilson, R.T. Franceschi, M.D. Morris, Tracking circadian rhythms of bone mineral deposition in murine calvarial organ cultures, J. Bone Miner. Res. 28 (2013) 1846–1854.
[20] F.A. Shah, A. Snis, A. Matic, P. Thomsen, A. Palmquist, 3D printed Ti6Al4V implant surface promotes bone maturation and retains a higher density of less aged osteocytes at the bone-implant interface, Acta Biomater. 30 (2016) 357–367.
[21] F.A. Shah, Micro-Raman spectroscopy reveals the presence of octacalcium phosphate and whitlockite in association with bacteria-free zones within the mineralized dental biofilm, Microsc. Microanal. 25 (2019) 129–134.
[22] F.A. Shah, B.E.J. Lee, J. Tedesco, C. Larsson Wexell, C. Persson, P. Thomsen, K. Grandfield, A. Palmquist, Micrometer-sized magnesium whitlockite crystals in micropetrosis of bisphosphonate-exposed human alveolar bone, Nano Lett. 17 (2017) 6210–6216.
[23] B. Depalle, Z. Qin, S.J. Shefelbine, M.J. Buehler, Large deformation mechanisms, plasticity, and failure of an individual collagen fibril with different mineral content, J. Bone Miner. Res. 31 (2016) 380–390.
[24] J.S. Yerramshetty, O. Akkus, The associations between mineral crystallinity and the mechanical properties of human cortical bone, Bone 42 (2008) 476–482.
[25] B. Wopenka, J.D. Pasteris, A mineralogical perspective on the apatite in bone, Mater. Sci. Eng. C Mater. Biol. Appl. 25 (2005) 131–143.
[26] C. Greenwood, J.G. Clement, A.J. Dicken, J.P.O. Evans, I.D. Lyburn, R.M. Martin, K.D. Rogers, N. Stone, G. Adams, P. Zioupos, The micro-architecture of human cancellous bone from fracture neck of femur patients in relation to the structural integrity and fracture toughness of the tissue, Bone Reports 3 (2015) 67–75.
[27] R.Z. Legeros, O.R. Trautz, J.P. Legeros, E. Klein, W.P. Shirra, Apatite crystallites: effects of carbonate on morphology, Science 155 (1967) 1409–1411.
[28] C. Gullekson, L. Lucas, K. Hewitt, L. Kreplak, Surface-sensitive Raman spectroscopy of collagen I fibrils, Biophys. J. 100 (2011) 1837–1845.
[29] B.G. Frushour, J.L. Koenig, Raman scattering of collagen, gelatin, and elastin, Biopolymers 14 (1975) 379–391.
[30] M. Janko, A. Zink, A.M. Gigler, W.M. Heckl, R.W. Stark, Nanostructure and mechanics of mummified type I collagen from the 5300-year-old Tyrolean Iceman, Proc. Biol. Sci. 277 (2010) 2301–2309.
[31] L. Knott, A.J. Bailey, Collagen cross-links in mineralizing tissues: a review of their chemistry, function, and clinical relevance, Bone 22 (1998) 181–187.
[32] S.P. Robins, Biochemistry and functional significance of collagen cross-linking, Biochem. Soc. Trans. 35 (2007) 849–852.
[33] E.P. Paschalis, D.N. Tatakis, S. Robins, P. Fratzl, I. Manjubala, R. Zoehrer, S. Gamsjaeger, B. Buchinger, A. Roschger, R. Phipps, A.L. Boskey, E. Dall'Ara, P. Varga, P. Zysset, K. Klaushofer, P. Roschger, Lathyrism-induced alterations in collagen cross-links influence the mechanical properties of bone material without affecting the mineral, Bone 49 (2011) 1232–1241.
[34] H.M. Frost, Micropetrosis, J. Bone Joint Surg. Am. 42-A (1960) 144–150.
[35] A. Boyde, The real response of bone to exercise, J. Anat. 203 (2003) 173–189.
[36] L.S. Bell, M. Kayser, C. Jones, The mineralized osteocyte: a living fossil, Am. J. Phys. Anthropol. 137 (2008) 449–456.
[37] B. Busse, D. Djonic, P. Milovanovic, M. Hahn, K. Puschel, R.O. Ritchie, M. Djuric, M. Amling, Decrease in the osteocyte lacunar density accompanied by hypermineralized lacunar occlusion reveals failure and delay of remodeling in aged human bone, Aging Cell 9 (2010) 1065–1075.
[38] E.G. Vajda, R.D. Bloebaum, Age-related hypermineralization in the female proximal human femur, Anat. Rec. 255 (1999) 202–211.
[39] V.T. Carpentier, J. Wong, Y. Yeap, C. Gan, P. Sutton-Smith, A. Badiei, N.L. Fazzalari, J.S. Kuliwaba, Increased proportion of hypermineralized osteocyte lacunae in osteoporotic and osteoarthritic human trabecular bone: implications for bone remodeling, Bone 50 (2012) 688–694.
[40] S. Aparicio, S.B. Doty, N.P. Camacho, E.P. Paschalis, L. Spevak, R. Mendelsohn, A.L. Boskey, Optimal methods for processing mineralized tissues for Fourier transform infrared microspectroscopy, Calcif. Tissue Int. 70 (2002) 422–429.